

Morphing Wing Flight Control Via Postbuckled Precompressed Piezoelectric Actuators

Roelof Vos* and Roeland De Breuker*

Delft University of Technology, 2629 HS Delft, The Netherlands

Ron Barrett†

University of Kansas, Lawrence, Kansas 66045

and

Paolo Tiso*

Delft University of Technology, 2629 HS Delft, The Netherlands

DOI: 10.2514/1.21292

The design, modeling, and testing of a morphing wing for flight control of an uninhabited aerial vehicle is detailed. The design employed a new type of piezoelectric flight control mechanism which relied on axial precompression to magnify control deflections and forces simultaneously. This postbuckled precompressed bending actuator was oriented in the plane of the 12% thick wing and mounted between the end of a tapered D-spar at the 40% chord and a trailing-edge stiffener at the 98% chord. Axial precompression was generated in the piezoelectric elements by an elastic skin which covered the outside of the wing and served as the aerodynamic surface over the aft 70% of the wing chord. A two-dimensional semi-analytical model based on the Rayleigh–Ritz method of assumed modes was used to predict the static and dynamic trailing-edge deflections as a function of the applied voltage and aerodynamic loading. It was shown that static trailing-edge deflections of ± 3.1 deg could be attained statically and dynamically through 34 Hz, with excellent correlation between theory and experiment. Wind tunnel and flight tests showed that the postbuckled precompressed morphing wing increased roll control authority on a 1.4 meter span uninhabited aerial vehicle while reducing weight, slop, part-count, and power consumption.

Nomenclature

A	=	extensional stiffness matrix or aspect ratio
B	=	coupled laminate stiffness matrix
b	=	span
C_L, C_l	=	three-dimensional, section lift coefficient
c	=	chord
D	=	bending laminate stiffness
E	=	total energy
F_a	=	aerodynamic force
F_0	=	precompression force
f	=	frequency
K	=	structural stiffness
\mathbf{K}	=	stiffness matrix
k	=	spring stiffness
L	=	actuator length
\mathbf{M}	=	applied moment vector
\mathbf{M}	=	mass matrix
m	=	mass
N	=	applied force vector
n	=	number of shape functions
P	=	lift force
p	=	pressure
q	=	amplitude
T	=	kinetic energy
t	=	thickness or time
U	=	internal energy or velocity
u	=	horizontal displacement

V	=	potential energy or voltage
w	=	vertical displacement
α	=	angle of attack
δ	=	trailing-edge deflection
ϵ	=	normal strain
θ	=	trailing-edge end rotation
κ	=	curvature
Λ	=	unloaded actuator strain
Π	=	potential energy
ρ	=	density
σ	=	normal stress
Φ	=	velocity potential
ϕ	=	disturbed velocity potential
ψ	=	shape function

Subscripts

a	=	actuator
b	=	bonding layer
c	=	circulatory
ex	=	external
h	=	hinge point
l	=	laminate
m	=	morphing part
nc	=	noncirculatory
sp	=	negative spring rate
t	=	thermal

Received 21 November 2005; revision received 4 April 2006; accepted for publication 22 May 2006. Copyright © 2006 by the authors. Published by the American Institute of Aeronautics and Astronautics, Inc., with permission. Copies of this paper may be made for personal or internal use, on condition that the copier pay the \$10.00 per-copy fee to the Copyright Clearance Center, Inc., 222 Rosewood Drive, Danvers, MA 01923; include the code 0021-8669/07 \$10.00 in correspondence with the CCC.

*Research Associate, Faculty of Aerospace Engineering, Department of Aerospace Structures, Kluyverweg 1. AIAA member.

†Associate Professor, Aerospace Engineering Department, 2120 Learned Hall. Senior AIAA Member.

Introduction

CONVENTIONAL roll control on aircraft is typically achieved by differential aileron deflection. By moving these small surfaces (generally between 10% and 30% of the local wing chord [1]) over a relatively large angle, the wing lift distribution is altered and the aircraft rotates about its longitudinal axis. Although effective and reliable when properly designed, these systems are relatively complex (with tens to hundreds of individual components), are heavy (weighing from 1.5 to 4% of an aircraft gross weight [2]), and

can add considerably to maintenance and inspection requirements. Additionally, they often have limited bandwidth, considerable power consumption, and/or require hard mechanical control connections through the length and span of the aircraft.

For more than a decade, a number of approaches have been made to improve flight control via adaptive aerostructures. From pitch active wings, to solid state flap mechanisms and rotors, these designs have been proven on the bench, in the wind tunnel, and eventually in flight [3–11]. In 1996, a detailed study on a subscale rotary-wing uninhabited aerial vehicle (UAV) showed that the flight control system weight could be reduced by as much as 40%, while simultaneously dropping the drag and power consumption [12–17]. In 2000, a new approach using all-moving wings was introduced. By employing shape-memory alloy filaments, it was shown that the pitch of two different wings could be altered, thereby generating large control forces [18]. Although these approaches worked quite well, they consumed so much power that the weight of the power supply doubled.

In lieu of rigid surface deflection or wing pitch manipulation, it is possible to use compliant materials in a deforming wing structure [19]. Over the past five years, extensive research has been done in the field of active wing deformation. Various approaches have been taken to actively change wing geometry: wing twisting, leading edge deformation, camber variation, planform area variation, tip bending, sweep variation, and wing folding [20–27]. Many of these efforts were tailored towards aircraft that change their external shape substantially to adapt to a changing mission environment during flight operations. Other studies showed that rolling performance could be enhanced by using conformal wing surfaces instead of conventional control surfaces [28,29]. It was demonstrated that wing morphing works well for membrane wings to induce roll control on small UAVs [30].

However, active deformation of wings with significant thickness often requires large control forces because not only do the air loads provide resistance, but also the inherent stiffness of the structure needs to be overcome. Using a conventional wing structure of ribs and spars consequently imposes stout requirements on the actuators which are to induce the wing deformation. If conventional actuators were used, this would imply that relatively heavy, bulky actuators would be needed to induce deformation.

However, instead of designing a structure with a high level of inherent stiffness, a compliant structure can be used so as to minimize the amount of energy invested in straining the passive structure. Of course, at the same time, the compliant wing has to provide sufficient strength and stiffness to sustain the aerodynamic loads.

Unlike earlier adaptive structures efforts, a new approach is needed to both provide large deflections like those that can be generated by shape memory alloy (SMA) systems, while maintaining the efficiency and speed of piezoelectric systems, all while keeping costs minimized. Although a host of “amplification” schemes, devices, and mechanisms have been conceived through the years, they have all traded force for deflection and in the process, incurred a finite loss of total work during this conversion along with an often substantial weight penalty. Accordingly, a simple mechanism is needed which magnifies both force and deflection while maintaining low weight and power consumption.

In an effort to satisfy these disparate requirements, a new class of actuators was conceived which takes advantage of newly developed structural actuator methodologies. In years past, most piezoelectric structures functioned with a driving equation that boiled down to: $F_{\text{piezo}} = K \Delta x$ where a comparatively small F_{piezo} fought against the passive stiffness of the structure K , to generate a deflection, Δx . Recently, however, a new class of piezoelectric elements called postbuckled precompressed (PBP) actuators changed all this [31,32]. These actuators are a subset of low net passive stiffness (LNPS) or zero net passive stiffness (ZNPS) class actuators and work on a fundamentally different principle: $F_{\text{piezo}} = (K - K_{\text{sp}}) \Delta x$ where K_{sp} is a negative spring rate mechanism and approaches K , thereby amplifying deflections for a given applied force level. It is these principles that can now be applied to thick wing sections to induce high deflections with minimal power consumption and weight.

A significant demonstration of this technology can show how elegant and powerful these fundamental techniques can be. This paper describes how structural morphing on a wing with finite thickness is applied to induce roll control on a subscale UAV. It will be shown that active deformation of the airfoil camber and thickness can be achieved with low resistance of a highly compliant wing skin.

The active deformation of the wing geometry is induced by integrating piezoelectric material in part of the wing structure. It will be shown that the integration of these adaptive materials can be done efficiently with a net weight savings. A semi-analytical model has been developed to predict the amount of wing deformation [33]. Static and dynamic bench tests were done to validate this model. Wind tunnel tests on a section of the wing quantitatively proved this concept of wing morphing. Finally, free flight tests were conducted to show that active camber variation ensures excellent roll control.

Morphing Wing Design and Fabrication

The proposed variable camber airfoil is based on the application of a new type of piezoelectric actuator which employs postbuckled precompressed bender elements. The PBP piezoelectric actuator is designed to have an increase in stroke by a factor of 2–4 with respect to the conventional bender actuators, depending on the voltage input and precompression level, while at the same time maintaining the amount of end force.

Advantages of PBP piezoelectric actuators over conventional electromechanical servoactuators for aircraft flight control have already been shown on the XQ-138, a subscale vertical takeoff and landing UAV. Significant weight, volume, and power consumption reductions were achieved, while at the same time actuation frequency was increased with an order of magnitude [31,34].

Increasing deflection of a normal bender element is induced by applying an axial force that loads the element in compression. Each deflection of the beam, initiated by the piezoelectric elements, is magnified by the compressive force. A compressive force close to the buckling load of the actuator can increase the deflections up to a factor of 4 with respect to the unloaded actuator [31]. The principle of the PBP actuators is extensively discussed by Barrett and Tiso [32] and follows from electrical transformer designs of Lesieutre and Davis [35].

From a performance point of view, the two main requirements on the deforming wing are a low drag increase upon wing morphing and a high change in lift. Furthermore, aeroelastic effects like flutter and divergence should not be encountered anywhere in the flight envelope of the aircraft. To develop a feasible and efficient design, additional requirements on the structural design of the wing were imposed: a low total wing weight (comparable to the weight of a conventional wing with servoactuated ailerons), low structural complexity, and sufficient structural strength and stiffness to sustain all the aerodynamic loads.

Applying the PBP actuator as a structural element in the wing put a few constraints on the wing geometry. One of these constraints was the fact that precompression of the actuator had to act exactly at the plane of symmetry of the actuator itself. This ensured that the actuator was capable of deflecting an equal amount up and down. Furthermore, there had to be a structural element(s) that made sure that the actuator was loaded in compression close to its buckling load.

From the set of requirements and constraints, a design was made for two deforming wing panels on a 1.4 m (55 in.) span high wing UAV. In this design, differential wing morphing of these panels induced a rolling moment about the aircraft's longitudinal axis. The cruise velocity for this aircraft was estimated to be 15 m/s. Figure 1 shows the design of the airfoil section. The PBP actuator was placed on the aft 60% of the camber line of a symmetric airfoil, based on a NACA 0012 geometry. The skin of the airfoil touched the PBP actuator at the trailing edge and provided the required amount of precompression. This implied that the skin had to be elastic such that it could act as an aerodynamic surface and at the same time as a precompression tool to increase the deflections of the actuator. The first 30% of the airfoil geometry was fixed and identical to the NACA 0012 airfoil geometry.

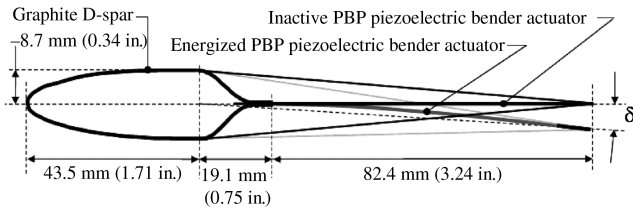


Fig. 1 Change airfoil camber due to PBP actuation.

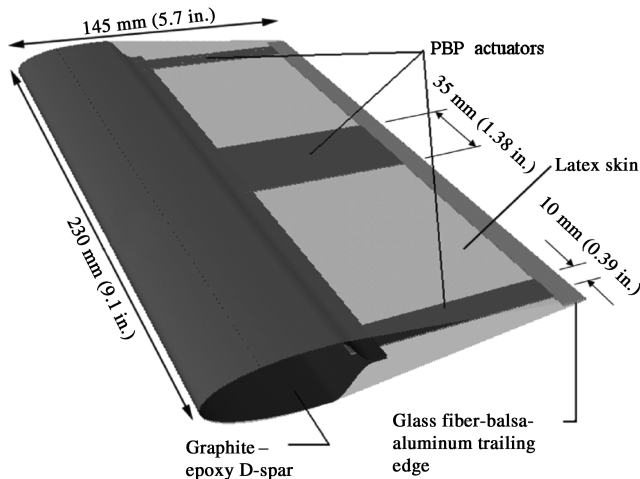


Fig. 2 Morphing wing panel employing PBP actuators on the camber line.

Each of the panels measured 145 mm (5.7 in.) in chord and 230 mm (9.1 in.) in width. To comply with the requirement of low structural complexity, the torque box structure of the wing was designed such that it would dictate the airfoil shape over the first 30% of the airfoil and at the same time act as a fixed structural element with sufficient stiffness to transfer the aerodynamic loads to the remaining (fixed) wing structure. As can be seen in Fig. 2, each deforming wing panel was composed of three PBP actuators, a graphite/epoxy D-spar, a composite trailing edge, and an elastic skin. This limited the total amount of components per morphing wing panel to only six.

Both morphing wing panels were positioned at the outboard sides of the wing. The remaining wing structure was composed of balsa wood spars and ribs which dictated the NACA 0012 shape. The wing did not possess any taper or sweep and the dihedral was 2 deg. The mean aerodynamic chord was 145 mm (5.7 in.) and its total width measured 1.4 m (55 in.). To protect the PBP elements from overrotating, at either side of the panel, bump stops were positioned. These bump stops allowed the trailing edge of the morphing wing panel to travel a maximum of 20 mm (0.78 in.) peak-to-peak in

vertical direction. At the outboard side, a winglet was positioned which protected the morphing wing panel during a heavy landing. Figure 3 shows how the morphing wing panels were integrated in the wing.

Morphing Wing Modeling

Semi-Analytical Structural Model

A semi-analytical model was developed, which predicted the amount of trailing-edge deflection as a function of voltage. Figure 4 shows how the morphing part of the airfoil was loaded by the skin (modeled by a spring with tension force F_0 and spring stiffness) and the aerodynamic end force, $(1/2)P_m$, which resulted from the pressure distribution over the airfoil. The trailing edge was modeled as a mass positioned at the end of the actuator.

Both the precompressive force and the aerodynamic end force influenced the amount of deflection of the piezoelectric actuator. It was already shown that when no compressive loading is present, classical laminated plate theory (CLPT) models predict the deflection of piezoelectric bender element very well [36]. The PBP actuator consisted of two conventionally attached piezoelectric sheets bonded to either side of a structurally stiff substrate. The total thickness of the laminate amounted to 0.635 mm (0.025 in.). When voltage was applied, the piezoelectric sheets alternatively expanded and contracted which induced bending in the element.

The resultant forces and moments in the laminate can be obtained by integrating the stress over the thickness of the laminate:

$$N = \int_{-t/2}^{t/2} \sigma dz \quad M = \int_{-t/2}^{t/2} \sigma z dz \quad (1)$$

The in-plane forces generated by the actuator are balanced by externally applied forces and moments, and forces and moments due to mismatch in coefficient of thermal expansion. As a result of these factors, in-plane laminate strains and curvatures occur:

$$\begin{pmatrix} N \\ M \end{pmatrix}_a + \begin{pmatrix} N \\ M \end{pmatrix}_{ex} + \begin{pmatrix} N \\ M \end{pmatrix}_l = \begin{bmatrix} A & B \\ B & D \end{bmatrix}_l \begin{pmatrix} \epsilon \\ \kappa \end{pmatrix}_l \quad (2)$$

For a bender element which is symmetric in both material properties as in geometry the amount of curvature is independent of the thermally induced stresses. Because in-plane strains due to thermally induced stresses are small, this term is neglected. The forces and moments in the laminate that are induced by the actuator elements are a function of the piezoelectric virgin strain Λ . Assuming no external loading, Eq. (2) can be written as

$$\begin{bmatrix} A & B \\ B & D \end{bmatrix}_a \begin{pmatrix} \Lambda \\ 0 \end{pmatrix}_a = \begin{bmatrix} A & B \\ B & D \end{bmatrix}_l \begin{pmatrix} \epsilon \\ \kappa \end{pmatrix}_l \quad (3)$$

Because of the symmetry in the laminate, the coupling stiffness is zero. For an unloaded element, the following relation between the free strain of the actuator and the curvature holds:

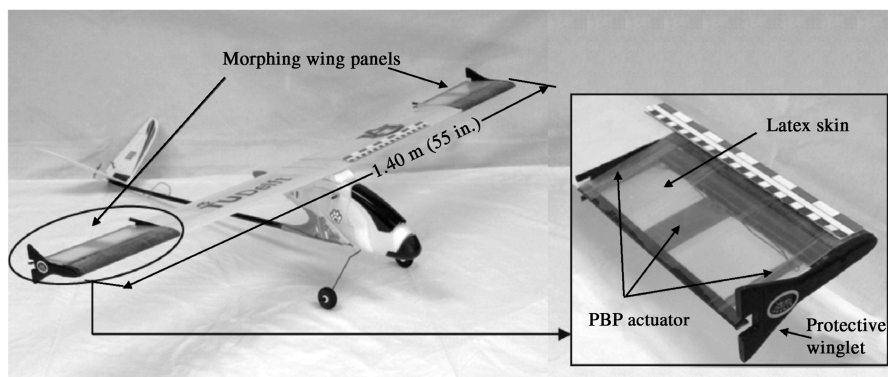


Fig. 3 UAV employing PBP actuated morphing panels.

$$\Lambda = \frac{D_l}{B_a} \kappa \quad (4)$$

The constant values for D_l and B_a can easily be calculated using CLPT theory. The free strain of the actuator in the laminate is one of the driving parameters of the eventual deflection of the morphing wing. If moderate rotations are assumed, the curvature is $\kappa = w''$. With w being the out-of-plane displacement of the actuator.

To predict the influence of external loading, the PBP actuator is modeled as an Euler–Bernoulli beam. The out-of-plane displacement is determined by the Rayleigh–Ritz method of assumed modes. Each assumed mode ψ_i is a shape function for the beam with a particular amplitude q_i . The out-of-plane displacement at spacial coordinate x and time t is prescribed by a summation over the number of assumed modes n :

$$w(x, t) = \sum_{i=1}^n q_i(t) \psi_i(x) \quad (5)$$

The mode shapes are expressed as polynomials that satisfy the essential boundary conditions at the root.

To describe the state of the laminate, the theory of minimum energy is used. The total energy is composed of the potential energy and kinetic energy:

$$E = \Pi + T \quad (6)$$

The potential energy is the sum of internal energy and external energy:

$$\Pi = U + V \quad (7)$$

The kinetic energy of the PBP actuator is expressed as follows:

$$T = \frac{1}{2} \int_0^L \rho_a \dot{w}^2 dx + \frac{1}{2} m [\dot{w}(L)]^2 \quad (8)$$

where ρ_a is the mass per unit length and unit width of the actuator, m is the mass per unit width of the trailing edge, and w is the out-of-plane displacement.

The expression for the strain energy U is as follows:

$$U = \int_V \sigma d\epsilon = \frac{1}{2} \int_0^L (N\epsilon + M w'') dx - \int_0^L B_a \Lambda w'' dx \quad (9)$$

N and M are the normal force and moment in the actuator. B_a and Λ correspond with the actuator nomenclature in Eq. (4).

Finally, the external energy, imposed by the skin force and by aerodynamic loading, can be written as

$$V = \frac{P_m}{2} w(L) - F_0(\Delta L_1 + \Delta L_2) + \frac{k}{2}(\Delta L_1^2 + \Delta L_2^2) \quad (10)$$

where

$$\Delta L_1 = \sqrt{[L + u(L) + x_0]^2 + [w(L) + z_0]^2} - \sqrt{(L + x_0)^2 + z_0^2} \quad (11)$$

$$\Delta L_2 = \sqrt{[L + u(L) + x_0]^2 + [w(L) - z_0]^2} - \sqrt{(L + x_0)^2 + z_0^2} \quad (12)$$

In Eq. (10), P_m is the lift force over the morphing part of the wing, and k is the stiffness of the skin. The dimensions x_0 and z_0 are displayed in Fig. 4. Because $u(L) \ll L$, $[u(L)/L]^2$ is neglected in Eqs. (11) and (12). The contribution of k to the total stiffness of the system is linearized around the equilibrium position where $w = 0$. The precompression force in the taut skin is much larger than the aerodynamic load. It is therefore assumed that the skin can be modeled as a membrane which will not exhibit any out-of-plane displacement due to the aerodynamic force. This results in a uniform stress distribution in the skin. Consequently, one-half of the lift force

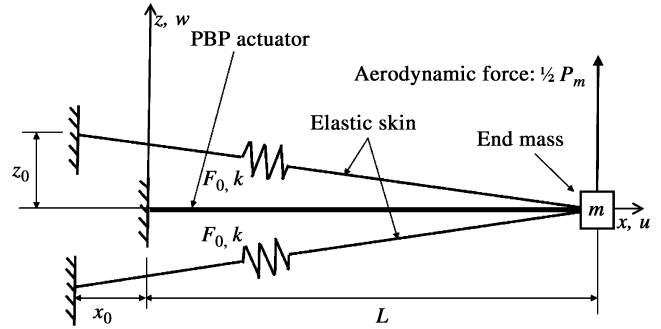


Fig. 4 Schematic representation of forces acting on the morphing part of the airfoil.

over the morphing part P_m is carried by the rigid part of the wing structure. The other half acts on the trailing edge. Furthermore, $u(L)$ and $w(L)$ are the displacements in x and z direction, respectively, at the length of the actuator.

Applying Lagrange’s equations, the state of the beam can be written as

$$\frac{d}{dt} \left(\frac{\partial T}{\partial \dot{q}} \right) - \frac{\partial T}{\partial q} + \frac{\partial U}{\partial q} = \frac{\partial V}{\partial q} \quad (13)$$

After substitutions, the governing equation takes the following matrix form

$$\mathbf{M} \ddot{q} + \mathbf{K} q = \mathbf{F}_a \quad (14)$$

The aerodynamic loading \mathbf{F}_a is expressed as

$$\mathbf{F}_a = \frac{P_m}{2} \psi(L) \quad (15)$$

The exact solution for the state of the beam is given in Eq. (13). This solution could be analytically solved for an infinite number of shape functions. In this model, the solution is approximated with a finite number n of shape functions. Figure 5 shows that the solution for maximum deflection converges at $n = 4$. For the frequency analysis, a convergence study was made for the first natural frequency as a function of the number of shape functions. Convergence of the solution was achieved at $n = 7$. However, the difference between the predicted natural frequency at $n = 1$ and $n = 7$ was only 0.5%.

Theodorsen’s Model

Because of the precompression of the bender elements the net stiffness of the morphing part of the structure decreased. Consequently, a pressure field over the airfoil section could induce

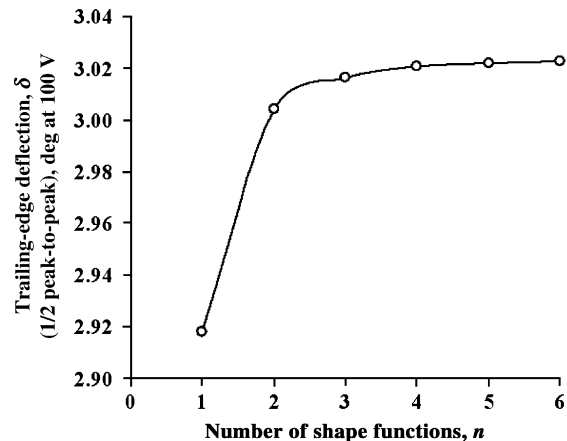


Fig. 5 Predicted maximum deflection vs number of shape functions.

substantial camber variations. The pressure distribution over the airfoil was modeled using Theodorsen's theory [37].

In this model, wing morphing induces a kink in the chord line (see Fig. 1). The flow over the airfoil is assumed to be incompressible, inviscid, and irrotational. This can be modeled by Laplace's equation [38]:

$$\nabla^2 \Phi = 0 \quad (16)$$

Following Theodorsen's theory [37], the velocity potential is expressed as a function of the perturbation velocity potential ϕ and the undisturbed flow velocity U :

$$\Phi = Ux + \phi \quad (17)$$

Substituting Eq. (17) in Eq. (16) yields

$$\nabla^2 \phi = 0 \quad (18)$$

To ensure flow tangency, the following boundary condition is imposed on the flow:

$$\frac{\partial \phi}{\partial z} = \frac{\partial w}{\partial t} + U \frac{\partial w}{\partial x} \quad (19)$$

In this flow tangency equation, w is the out-of-plane displacement of the camber line and U is the undisturbed flow velocity.

The pressure distribution Δp over the airfoil is divided into two parts, a *circulatory* and a *noncirculatory* part. The circulatory part is associated with the wake. As a consequence, the net pressure distribution becomes

$$\Delta p = \Delta p_c + \Delta p_{nc} \quad (20)$$

Consistent with thin airfoil theory, the flow that induces the noncirculatory pressure distribution is modeled using a distribution of sources and sinks on the chord line. Using conformal mapping, a solution of Laplace's equation for the disturbed velocity potential can be obtained [39]. With this solution, the noncirculatory pressure increment can be deduced using the unsteady Bernoulli equation:

$$\Delta p_{nc} = -2\rho \left(\frac{\partial \phi}{\partial t} + U \frac{\partial \phi}{\partial x} \right) \quad (21)$$

where ρ is the density of the surrounding air. Because incompressible flow is assumed, the density is constant.

The circulatory pressure is determined by applying the Kelvin circulation theorem and enforcing the Kutta condition on the airfoil-wake combination. Assuming that a vortex at location x_0 in the wake moves with the undisturbed flow velocity U , the following relation holds:

$$\frac{\partial \phi}{\partial t} = U \frac{\partial \phi}{\partial x_0} \quad (22)$$

By using Bernoulli's equation for unsteady incompressible flow, this results in the following circulatory pressure distribution:

$$\Delta p_c = -2\rho U \left(\frac{\partial \phi}{\partial x_0} + \frac{\partial \phi}{\partial x} \right) \quad (23)$$

The kink in the chord line can be modeled as a flap that starts with a hinge point at 30% of the chord. It is assumed that the flow is steady. Consequently, Theodorsen's function, $C(k) = 1$. The resulting lift force over the entire airfoil can then be written as [37]

$$P = \int_0^c \Delta p \, dx = 2\pi \frac{\rho U^2 c}{2} \left(\alpha + \frac{T_{10}}{\pi} \delta \right) \quad (24)$$

with T_{10} being one of Theodorsen's constants:

$$T_{10} = \sqrt{1 - \left(\frac{2x_h - c}{c} \right)^2} + \cos^{-1} \left(\frac{2x_h - c}{c} \right) \quad (25)$$

For the lift force that acts at the center of pressure of the morphing part P_m , the following holds:

$$P_m = \int_{x_h}^c \Delta p \, dx = 2\pi \frac{\rho U^2 c}{2} \cos^{-1} \left(\frac{2x_h - c}{c} \right) \left(\alpha + \frac{T_{10}}{\pi} \delta \right) \quad (26)$$

where x_h is the hinge point of the morphing part [$x_h = 43.5$ mm (1.71 in.), see Fig. 4].

Vortex Lattice Model

To show the validity of the semi-analytical predictions of the morphing wing panel in a flow field, the MATLAB based vortex lattice program Tornado was used. Tornado uses standard vortex lattice theory, stemming from potential flow theory. In this code, however, the standard horseshoe vortex is replaced by a vortex sling arrangement. This basically works in the same way as the horseshoe, with the exception that the legs of the horseshoe are flexible and consist of seven (instead of three) vortices of equal strength. This enables a more accurate prediction of flapped panels [40].

The morphing wing panel was modeled as a straight wing with a NACA 0012 airfoil and a hinge point at 30% chord. In the semi-analytical model, the voltage over the piezoelectric sheets and the aerodynamic loads (triggered by the angle of attack) determined the amount of trailing-edge deflection. In this model, however, trailing-edge deflection in combination with the angle of attack determined the amount of lift over the panel. It is for this reason that the vortex lattice model was used solely to verify the predictions of the semi-analytical model, rather than to predict the amount of trailing-edge deflection that could be attained with the PBP actuators.

Experimental Testing and Results

Skin Tests

One of the key features in the design of this deforming wing structure was the skin. The skin was made out of natural rubber and was continuous over the entire perimeter of the airfoil. The skin was pre-tensioned such as to induce the required amount of precompression to the PBP actuators. At the same time, the skin acted as a nonreinforced aerodynamic surface for 70% of the airfoil chord.

To determine the amount of precompression force that the skin would generate, a skin sample was elongated using a strain measurement device that could measure elongations with an accuracy of 0.0254 mm (0.001 in.). Force levels were recorded using a scale with an accuracy of ± 0.5 gmf. The skin sample was a continuous band which measured 25 microns (0.0010 in.) in thickness, 20 mm (0.79 in.) in width, and its initial (no strain) length was 51 mm (2.01 in.). The measurement procedure was as follows: the skin sample was elongated with increments of 12.7 mm (0.5 in.) until a maximum length of 177.8 mm (7.0 in.). At every elongation increment, the tensional force was measured after a settling time of 5 min. After maximum elongation was reached, the skin was relaxed in steps of 12.7 mm (0.5 in.) and the same procedure for recording the force was applied.

Strain was defined to be the fraction of length of the skin over its original length (no tension applied). During the experiments, the skin was allowed to contract laterally without being constrained. It was assumed that natural rubber is incompressible and that the total volume of the skin remained constant. Furthermore, it was assumed that the material is isotropic and that lateral contraction was equal in thickness as well as in width direction of the specimen. Under these assumptions, the width of the specimen b is a function of the strain and the initial width b_0 :

$$b = \frac{1}{\sqrt{1 + \epsilon}} b_0 \quad (27)$$

The specific precompression force was defined to be the measured force F_m per unit width of the sample:

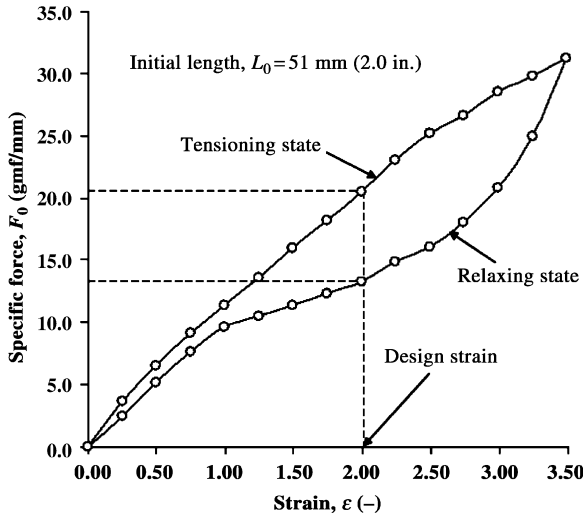


Fig. 6 Relation between specific precompression force F_0 and strain ϵ .

$$F_0 = \frac{F_m}{b} \quad (28)$$

Figure 6 shows the relation between the strain and the specific precompression force. Two lines are shown, one for the tensioning state and one for the relaxing state. From the airfoil geometry, it was determined that the required strain in the skin amounted to 2.0, which corresponded to a precompression force between 20.50 gmf/mm (1.146 lb/in.) and 13.32 gmf/mm (0.744 lb/in.), depending on whether the skin was being tensioned or relaxed.

For analysis, the pre-tensioning force and the stiffness were required. To simplify the analysis, the pre-tensioning force in the skin was assumed to be the exact average of the force acquired in the tensioning state and the force acquired in the relaxing state. Furthermore, the stiffness, which could be deduced from the derivative of the force-strain graph, was also averaged over the tensioning and relaxing state. Accordingly, the assumed precompression force per unit length was 16.91 gmf/mm (0.9449 lb/in.) and the assumed stiffness per unit length amounted to 0.128 gmf/mm² (0.182 lb/in²). Integrating this over the entire width of the morphing part [$b_m = 230$ mm (9.06 in.)] and dividing it by the total width of the PBP actuators [$b_a = 55$ mm (2.3 in.)] resulted in a precompression force per unit width of the actuator of 70.7 gmf/mm (3.95 lb/in.) and a spring stiffness per unit length of the actuator of 0.534 gmf/mm² (0.758 lb/in²). These values were the input parameters for the structural model.

Quasi-Static and Dynamic Bench Tests

Trailing-edge deflections induced by the PBP actuator were measured using quasi-static bench tests. Figure 7 shows the test setup of the wing panel, clamped in two vises at either side. A laser beam was reflected off the trailing edge of the wing and projected onto a reflection board. Trailing-edge end rotation angles could be measured with an accuracy of 0.062 deg. A signal generator (not depicted) generated a sine wave voltage signal of a given frequency, which was amplified by a voltage amplifier. The kinematic relation between the amount of trailing-edge deflection and end rotation is as follows:

$$\delta = \tan^{-1} \left(\frac{\tan(\theta/2)}{L + x_0} \right) \quad (29)$$

Measurements were taken at a constant frequency of 1 Hz (± 0.05). Peak-to-peak voltage levels were measured with an accuracy of ± 0.5 V using a multimeter. The results of these measurements are shown in Fig. 8a.

From Fig. 8a, it can be observed that maximum trailing-edge deflection amounted to 3.1 deg. The semi-analytical structural model

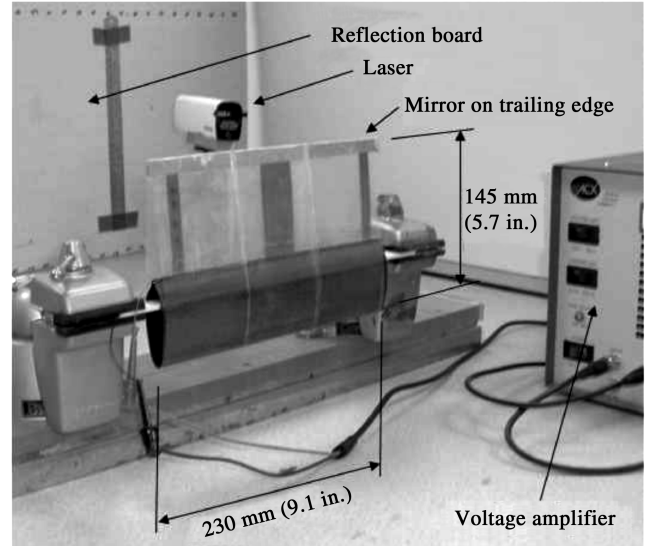


Fig. 7 Experimental setup for measuring of trailing-edge end rotations.

showed excellent correlation with the measured values. The modeled results were obtained for $n = 4$ number of shape functions.

Dynamic tests were carried out to find the natural frequency and break frequency of the wing panel. Precompression of the actuators reduced the net stiffness of the structure, which meant that the resonance frequency decreased. A frequency sweep at low voltage was carried out to record the amount of deflections at a peak-to-peak voltage level of 13.5 V (± 0.05).

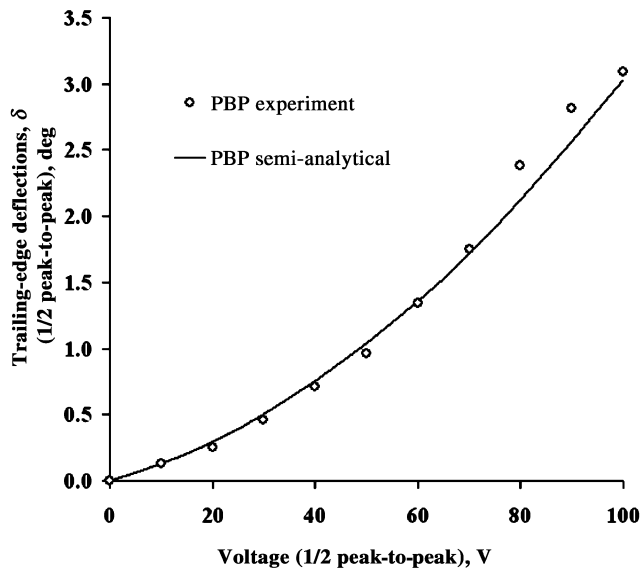
To compare the bandwidth of the PBP actuators to the bandwidth of high-performance submicro servoactuators, the deflections were normalized with respect to the static deflections. Figure 8b shows the normalized deflection δ plotted against the frequency. The first natural frequency occurred at 26 Hz. It can be seen that the semi-analytical prediction showed good correlation with the experimental values. The break frequency for this morphing wing amounted to 34 Hz, which was more than an order of magnitude higher than for conventional servoactuators (3 Hz). Because no damping was assumed, the predicted natural frequency peak was considerably higher than the one that was determined from experiment. The predicted results were obtained with $n = 7$ number of shape functions.

Wind Tunnel Tests

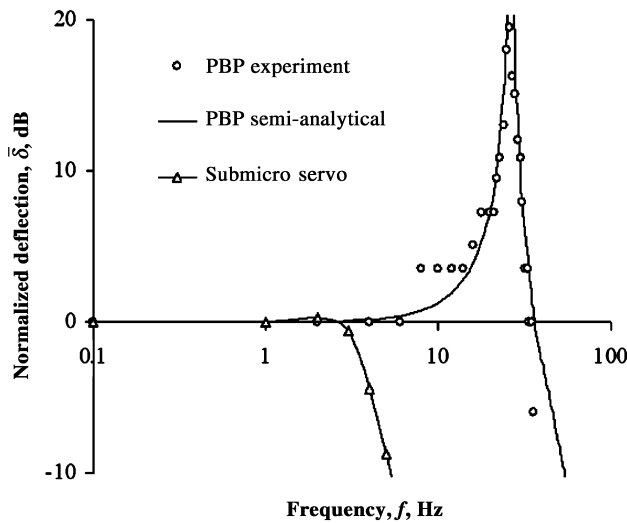
Wind tunnel tests on the deforming wing panel were carried out in the Dobbonga open vertical wind tunnel at Delft University of Technology. Lift could be measured with an accuracy of 0.5 gmf (0.001 lb). Lift measurements were taken at a constant wind velocity of 15 m/s. Velocity was deduced from difference in static pressure and total pressure (measured by a pitot tube in the flow). The total pressure could be measured with an accuracy of ± 0.5 Pa (0.02 lb/ft²) at a dynamic pressure of 138 Pa (2.88 lb/ft²). The angle of attack of the wing could be determined with an accuracy of ± 0.05 deg. Figure 9 shows the test article positioned in the vertical wind tunnel.

The wing was tested at three different angles of attack: 0, 5, and 10 deg. At each position, a voltage sweep was carried out from 0 to 100 V in steps of 10 V (± 0.5 deg). At each voltage point, both lift force and deflection were recorded. From these parameters, a relation is plotted between the lift coefficient C_L and the trailing-edge deflection in Fig. 10.

In Fig. 10, both the results from the wind tunnel experiment and the predicted values that follow from the semi-analytical model are shown. To correct the semi-analytically predicted lift coefficients for three dimensionality, the following reduced Polhamus equation is used [41]:



a) Trailing-edge deflection, δ vs voltage, V



b) Relation between the excitation frequency, f and normalized deflection, $\bar{\delta}$

Fig. 8 Static and dynamic bench test results.

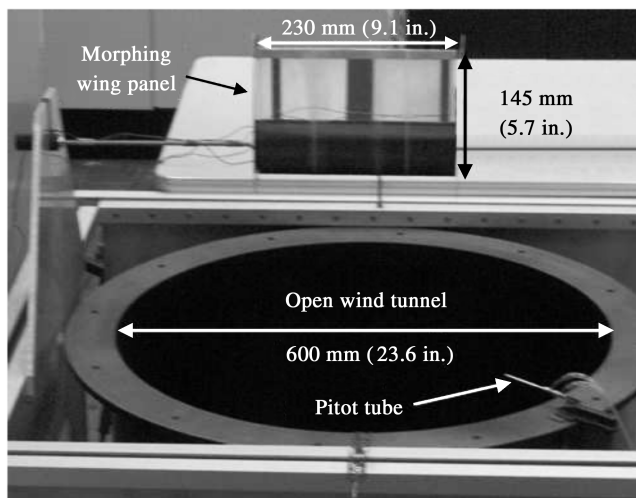


Fig. 9 Wind tunnel test article in vertical wind tunnel.

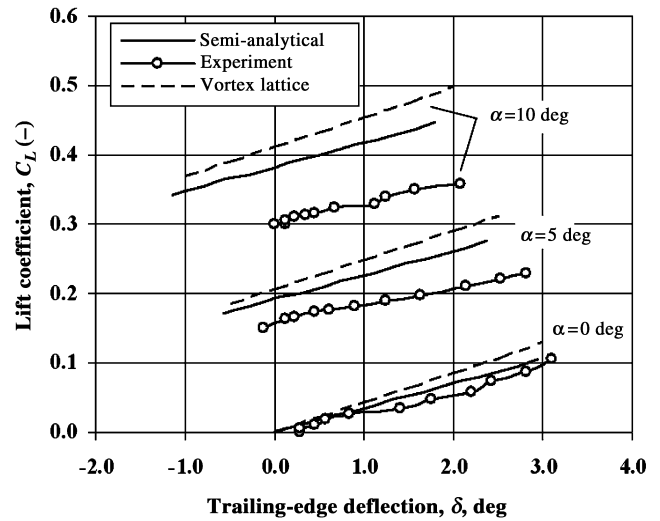


Fig. 10 Lift coefficient vs trailing-edge deflection at various angles of attack.

$$C_L = \frac{A}{2 + \sqrt{A^2 + 4}} C_l \quad (30)$$

The correlation between the semi-analytic prediction and the wind tunnel experiments is limited to small angles of attack. It can be seen from Fig. 10 that the discrepancy between the semi-analytical value of lift coefficient and the measured value increases with angle of attack. A cause for this disparity is thought to originate from tip-relieving (which degrades effective angle of attack), aerostructural interaction, blow-by (in the slots around the surface), and curvilinear surface flow separation.

From Fig. 10, similar trend lines can be seen for the measured values of the lift coefficient and the predicted values by the analytical model and the vortex lattice model. The average measured $C_{L\delta}$ (lift coefficient differentiated with respect to trailing-edge deflection) amounts to $C_{L\delta} = 1.72(1/\text{rad})$ and is 17% off with respect to the predicted value of $C_{L\delta} = 2.02(1/\text{rad})$ (semi-analytical) and 30% off with respect to the vortex lattice prediction ($C_{L\delta} = 2.44(1/\text{rad})$). Reasons such as flow angularity in the tunnel, flexibility of the model, and tunnel wall effects could have caused this change in the lift curve slope. More accurate wind tunnel tests and analytical modeling are required to improve the correlation between experiment and the semi-analytical model.

From Fig. 10, it can be observed that the $C_L - \delta$ lines shift backwards at higher angles of attack (both experiment and model show this behavior). This shift is caused by the higher aerodynamic force P_m on the actuator. This force will induce an initial deflection of the actuators when no voltage is applied. Because blocked force is traded for deflection, the actuators will show less deflection in opposite direction to the aerodynamic force.

Flight Tests

To remotely control the aircraft during flight, a dedicated electronic circuit was designed and manufactured. The circuit consisted of one direct current converter (PICO 5A48D) in combination with two OPA445 Op-Amps. This circuit was positioned between a conventional radio control receiver and the PBP actuators, and could transform the pulse-width modulated 5 V signal into a variable direct current signal which could range between -95 and $+95$ V.

Successful flight testing was carried out on 29 April 2005 in Auburn, AL under light and variable 5 kn winds, 15°C (59°F), and 7 statute miles of visibility. Flight tests showed excellent roll control. Figure 11 shows the aircraft just after takeoff.

From video footage of the flight tests, roll accelerations were determined which could be translated to rolling moment coefficients. The flight testing demonstrated that the PBP system control

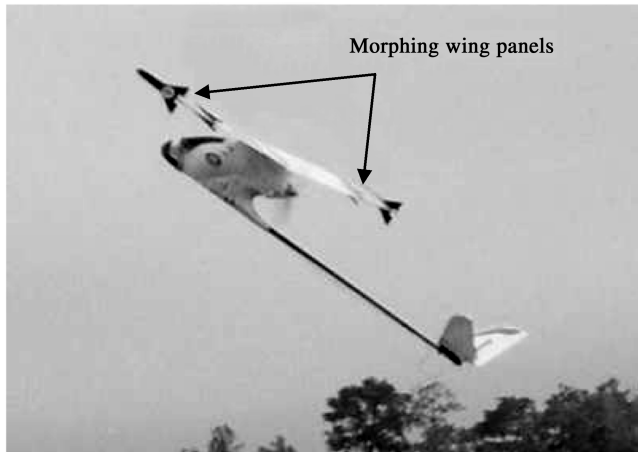


Fig. 11 PBP actuated morphing wing in flight.

derivatives were 3.7 times greater than conventional ailerons on the stock wing [41] and that the maximum control authority was increased 38% with respect to the conventional system.

Integration Characteristics and Comparison

The application of the morphing wing panels to induce roll control had clear advantages over conventional ailerons in combination with electromechanical servoactuators. Because the PBP actuators did not employ any linkages, gears, or heavy motors, they were therefore significantly lighter. The PBP actuators operated under a high voltage but very low current, and so power consumption was decreased substantially [42]. This could in turn lead to a reduction in battery capacity and consequently, battery weight.

A weight comparison was made between the six PBP actuators that controlled the two morphing wing panels, and a high-performance submicro servoactuator driving two ailerons on a wing of identical size. The result of this comparison is shown in Fig. 12. The comparison shows that operating empty weight could be reduced by almost 3.5% when switching from conventional aileron actuators to PBP actuated morphing wings.

It is emphasized that the comparison presented in Fig. 12 is confined to subscale UAVs. Applying PBP morphing technology to full-scale aircraft will require a new weight assessment. If weight is the principal driver for choosing a particular control system, the flight control system weight fraction of both conventional actuators and PBP actuators should be carefully evaluated and compared. If conventional actuators show lower levels of flight control system weight they should be preferred over PBP actuators and vice versa. Future work will be done to show at which scale this crossover between these different flight control systems occurs.

Contradictory to conventional servoactuators, the PBP actuator is solid state so part-count, slop, and deadband are one to two orders of magnitude lower [31,43]. As was shown in Fig. 8b, a PBP actuated morphing wing can increase the actuation frequency by more than an order of magnitude, with excellent control authority.

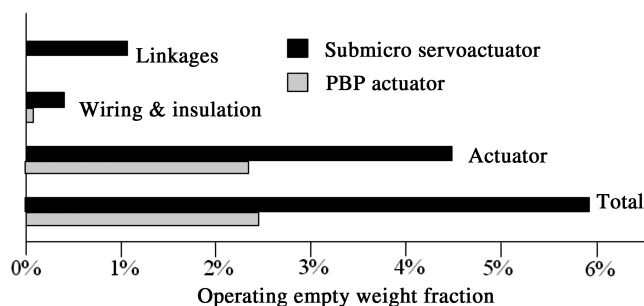


Fig. 12 Comparison of PBP and conventional servoactuator operating empty weight fractions for subscale UAV.

Conclusions

It has been shown that a PBP actuated morphing wing can be successfully applied to induce roll control on a subscale UAV morphing wing. A semi-analytical model based on the Rayleigh–Ritz method of assumed modes was developed to predict the amount of wing morphing as a function of the applied electric field on the piezoelectric actuator elements. Aerodynamic loading on the wing was modeled using Theodorsen’s theory of disturbed flow. Static and dynamic bench tests have shown a maximum deflection of more than ± 3 deg up to a break frequency of 34 Hz, with excellent correlation between theory and experiment. Wind tunnel tests have proven quantitatively that wing morphing induced by the PBP actuators results in a change in lift coefficient. At low angles of attack, the semi-analytical model showed good correlation with the measurements. Free-flight tests have demonstrated that a subscale uninhabited aircraft employing morphing wing panels at the outboard side of the wing shows excellent roll control upon wing morphing. With respect to conventional electromechanical servoactuators, applying PBP actuators leads to a saving in operating empty weight by 3.5% and an increase in break frequency from 3–34 Hz. Future work will be tailored toward the scalability of this technology toward full-scale aircraft.

Acknowledgments

The authors would like to acknowledge the Delft University of Technology Faculty of Aerospace Engineering and the Auburn University Aerospace Engineering Department for supporting this research. Special thanks to Mostafa Abdalla, Leo Veldhuis, Lars Krakkers, Michel van Tooren, and Zafer Gürdal. The authors would also like to thank Christoph Burger for piloting the aircraft and for his consistent support and assistance.

References

- [1] Roskam, J., *Airplane Design, Part 2: Preliminary Configuration Design and Integration of the Propulsion System*, DARCorp, Lawrence, KS, 2006.
- [2] Roskam, J., *Airplane Design, Part 5: Component Weight Estimation*, Chap. Flight Control System Weight Estimation, DARCorp, Lawrence, KS, 1989.
- [3] Barrett, R., “Intelligent Rotor Blade and Structures Development Using Directionally Attached Piezoelectric Crystals,” M.S. Thesis, Univ. of Maryland, College Park, MD, 1990.
- [4] Kudva, J. N., “Overview of the DARPA Smart Wing Project,” *Journal of Intelligent Material Systems and Structures*, Vol. 15, No. 4, April 2004, pp. 261–267.
- [5] Sanders, B., and Kudva, J. N., “Overview of the DARPA/AFRL Next Generation Morphing Aircraft Structures (N-MAS) Program,” *Proceedings of the 11th Annual International Symposium on Smart Structures and Materials*, Society of Photo-Optical Instrumentation Engineers Paper 5388-22, San Diego, CA, March 2004.
- [6] Barrett, R., Gross, R. S., and Brozoski, F., “Missile Flight Control Using Active Flexspar Actuators,” *Smart Materials and Structures*, Vol. 5, No. 2, April 1996, pp. 121–128.
- [7] Sanders, B., Crowe, R., and Garcia, E., “Defense Advanced Research Projects Agency: Smart Materials and Structures Demonstration Program Overview,” *Journal of Intelligent Material Systems and Structures*, Vol. 15, No. 4, April 2004, pp. 227–233.
- [8] Sanders, B., Cowan, D., and Scherer, L., “Aerodynamic Performance of the Smart Wing Control Effectors,” *Journal of Intelligent Material Systems and Structures*, Vol. 15, No. 4, April 2004, pp. 293–303.
- [9] Barrett, R., Gross, R. S., and Brozoski, F., “Design and Testing of Subsonic All-Moving Smart Flight Control Surfaces,” *Proceedings of the 36th AIAA Structures, Structural Dynamics and Control Conference*, AIAA Paper 95-1081, New Orleans, LA, April 1995, pp. 2289–2296.
- [10] Kennedy, D. K., Strau, F., Schetky, L. M., Chaudhry, Z., and Roznoy, R., “Development of an SMA Actuator for In-Flight Rotor Blade Tracking,” *Journal of Intelligent Material Systems and Structures*, Vol. 15, No. 4, April 2004, pp. 235–248.
- [11] Bartley-Cho, J. D., Wang, D. P., Martin, C. A., and Kudva, J. N., “Development of High-Rate, Adaptive Trailing Edge Control Surface for the Smart Wing Phase 2 Wind Tunnel Model,” *Journal of Intelligent*

- Material Systems and Structures*, Vol. 15, No. 4, April 2004, pp. 279–291.
- [12] Barrett, R., and Stutts, J., “Design and Testing of a 1/12th Scale Solid State Adaptive Rotor,” *Smart Materials and Structures*, Vol. 6, No. 4, Aug. 1997, pp. 491–497.
- [13] Ehlers, S., and Weisshaar, T., “Static Aeroelastic Behavior of an Adaptive Laminated Piezoelectric Composite Wing,” *Proceedings of the 31st AIAA/ASME/ASCE/AHS/ASC Structures, Structural Dynamics and Materials Conference*, AIAA Paper 90-1078, 1990.
- [14] Ehlers, S., and Weisshaar, T., “Effect of Adaptive Material Properties on Static Aeroelastic Control,” *Proceedings of the 33rd AIAA/ASME/ASCE/AHS/ASC Structures, Structural Dynamics and Materials Conference*, AIAA Paper 92-2526, April 1992.
- [15] Barrett, R., “Method and Apparatus for Structural Actuation and Sensing in a Desired Direction,” U.S. Patent 5,440,193, Aug. 1995.
- [16] Barrett, R., “Active Plate and Wing Research Using EDAP Elements,” *Smart Materials and Structures*, Vol. 1, June 1992, pp. 214–226.
- [17] Barrett, R., “Adaptive Aerostructures: The First Decade of Flight on Uninhabited Aerospace Systems,” *Proceedings of the Society of Photo-Optical Instrumentation Engineers 11th Annual International Symposium on Smart Structures and Materials*, Vol. 5388, Society of Photo-Optical Instrumentation Engineers, Bellingham, WA, Sept. 2004, pp. 190–201.
- [18] Barrett, R., Burger, C., and Melian, J., “Recent Advances in Uninhabited Aerial Vehicle (UAV) Flight Control with Adaptive Aerostructures,” *Proceedings of the 2001 Conference on Smart Technology Demonstrators and Devices*, Inst. of Physics Publishing, London, June 2002, pp. 1–11.
- [19] Kota, S., Hetricka, J., Osborna, R., Paulb, D., Pendletonb, E., Flickb, P., and Tilmannb, C., “Design and Application of Compliant Mechanisms for Morphing Aircraft Structures,” *Proceedings of SPIE Smart Structures and Materials*, Vol. 5054, Society of Photo-Optical Instrumentation Engineers, Bellingham, WA, Aug. 2003, pp. 24–33.
- [20] Gano, S. E., and Renaud, J. E., “Optimized Unmanned Aerial Vehicle with Wing Morphing for Extended Range and Endurance,” *Proceedings of the 9th AIAA/ISSMO Symposium and Exhibit on Multidisciplinary Analysis and Optimization*, AIAA Paper 2002-5668, 2002.
- [21] Gano, S. E., Renaud, J. E., Batill, S. M., and Tovar, A., “Shape Optimization for Conforming Airfoils,” *Proceedings of 44th AIAA/ASME/ASCE/AHS Structures, Structural Dynamics, and Materials Conference*, AIAA Paper 2003-1579, 2003, pp. 1–10.
- [22] Gern, F. H., Inman, D. J., and Kapania, R. K., “Structural and Aeroelastic Modeling of General Planform Wings with Morphing Airfoils,” *AIAA Journal*, Vol. 40, No. 4, 2002, pp. 628–637.
- [23] Bharti, S., Frecker, M., Lesieutre, G., and Ramrakhiani, D., “Active and Passive Material Optimization in a Tendon Actuated Morphing Aircraft Structure,” *Proceedings of Society of Photo-Optical Instrumentation Engineers Smart Structures and Materials*, Vol. 5390, 2004, pp. 247–257.
- [24] Rusnell, M. T., Gano, S. E., Perez, V. M., Renaud, J. E., and Batill, S. M., “Morphing UAV Pareto Curve Shift for Enhanced Performance,” *Proceedings of the 45th AIAA/ASME/ASCE/AHS/ASC Structures, Structural Dynamics and Materials Conference*, AIAA Paper 2004-1682, 2004, pp. 1–15.
- [25] Neal, D. A., Good, M. G., Johnston, C. O., Robertshaw, H. H., Mason, W. H., and Inman, D. J., “Design and Wind-Tunnel Analysis of a Fully Adaptive Aircraft Configuration,” *Proceedings of the 45th AIAA/ASME/ASCE/AHS/ASC Structures, Structural Dynamics and Materials Conference*, AIAA Paper 2004-1727, 2004.
- [26] Jha, A. K., and Kudva, J. N., “Morphing Aircraft Concepts, Classifications, and Challenges,” *Proceedings of SPIE Smart Structures and Materials*, Vol. 5388, Society of Photo-Optical Instrumentation Engineers, Bellingham, WA, 2004, pp. 213–224.
- [27] Lee, D., and Weisshaar, T. A., “Aeroelastic Studies on a Folding Wing Configuration,” *Proceedings of 46th AIAA/ASME/ASCE/AHS/ASC Structures, Structural Dynamics and Materials Conference*, AIAA Paper 2005-1996, 2005, pp. 1–13.
- [28] Sanders, B., Eastep, F. E., and Forster, E., “Aerodynamic and Aeroelastic Characteristics of Wings with Conformal Control Surfaces for Morphing Aircraft,” *Journal of Aircraft*, Vol. 40, No. 1, Jan.–Feb. 2003, pp. 94–99.
- [29] McGowan, A.-M. R., Washburn, A. E., Horta, L. G., Bryant, R. G., Cox, D. E., Siochi, E. J., Padula, S. L., and Holloway, N. M., “Recent Results from NASA’s Morphing Project,” *Proceedings of SPIE Smart Structures and Materials*, Vol. 4698, Society of Photo-Optical Instrumentation Engineers, Bellingham, WA, 2002, pp. 97–111.
- [30] Garcia, H., Abdulrahim, M., Lind, R., “Roll Control for a Micro Air Vehicle Using Active Wing Morphing,” *Proceedings of AIAA Guidance, Navigation, and Control Conference and Exhibit*, AIAA Paper 2003-5347, 2003.
- [31] Barrett, R., McMurtry, R., Vos, R., Tiso, P., and DeBreuker, R., “Postbuckled Precompressed (PBP) Elements: A New Class of Flight Control Actuators Enhancing High Speed Autonomous VTOL MAVs,” Society of Photo-Optical Instrumentation Engineers No. 5762-16, San Diego, CA, 6–10 March 2005.
- [32] Barrett, R., and Tiso, P., “PBP Adaptive Actuator Device and Embodiments,” International Patent Application PCT/NL2005/000054 by Delft Univ. of Technology, 18 Feb. 2005.
- [33] DeBreuker, R., Tiso, P., Vos, R., and Barrett, R., “Nonlinear Semi-Analytical Modeling of Postbuckled Precompressed (PBP) Piezoelectric Actuators for UAV Flight Control,” *47th AIAA/ASME/ASCE/AHS/ASC Structures, Structural Dynamics and Materials Conference*, AIAA Paper 2006-1795, 2006.
- [34] Barrett, R., Vos, R., Tiso, P., and DeBreuker, R., “Postbuckled Precompressed (PBP) Actuators: Enhancing VTOL Autonomous High Speed MAVs,” *Proceedings of the 46th AIAA/ASME/ASCE/AHS/ASC Structures, Structural Dynamics and Materials Conference*, AIAA Paper 2005-2113, 2005.
- [35] Lesieutre, G., and Davis, C., “Can a Coupling Coefficient of a Piezoelectric Actuator be Higher than Those of its Active Material?” *Journal of Intelligent Material Systems and Structures*, Vol. 8, No. 10, 1997, pp. 859–867.
- [36] Barrett, R., Frye, P., and Schliesman, M., “Design, Construction and Characterization of a Flightworthy Piezoelectric Solid State Adaptive Rotor,” *Smart Materials and Structures*, Vol. 7, No. 3, 1998, pp. 422–431.
- [37] Theodorsen, T., “General Theory of Aerodynamic Instability and the Mechanism of Flutter,” NASA, TR 496, 1935.
- [38] Anderson, J., *Fundamentals of Aerodynamics*, 2nd ed., McGraw–Hill, New York, 1991.
- [39] Bisplinghoff, R., and Ashley, H., *Principles of Aeroelasticity*, Dover, New York, 1962.
- [40] Melin, T., “Tornado, a Vortex Lattice MATLAB Implementation for Linear Aerodynamic Wing Applications,” M.S. Thesis, Royal Inst. of Technology, Stockholm, Sweden, Dec. 2000.
- [41] Roskam, J., “Stability, Control, and Hinge Moment Derivatives,” *Airplane Design, Part 6: Preliminary Calculation Aerodynamic, Thrust and Power Characteristics*, DARCorp, Lawrence, KS, 1990.
- [42] Bramlette, R., and Leurck, R., “Method for Control Surface Deflection Utilizing Piezoceramic Bimorph Actuators,” *Proceedings of the 44th AIAA Aerospace Sciences Meeting and Exhibit*, AIAA Paper 2006-143, 2006.
- [43] Vos, R., Barrett, R., Krakkers, L., and van Tooren, M., “Postbuckled Precompressed (PBP) Piezoelectric Actuators for UAV Flight Control,” Society of Photo-Optical Instrumentation Engineers No. 6173-15, San Diego, CA, 2006.